ADVANCED FUNCTIONAL MATERIALS
www.afm-journal.de

Magnetocaloric-Responsive Hydrogel Nanoarchitectonics for Pyroptosis-Relay-Immunotherapy to Suppress Post-Operation Tumor Recurrence and Metastasis

Siyu Wang, Huaqing Jing, Rui Yang, Zbynek Heger, Sona Krizkova, Yue Zhou, Xiaoyang Liang, Vojtech Adam, and Nan Li**

Although a widely used option in contemporary anticancer treatment, surgery still causes serious issues, including post-operation recurrence and the development of metastases. Immunotherapy, often following surgical resection of a tumor, has demonstrated benefits in improving the therapeutical outcomes of surgery. However, antigen generation and presentation play an essential role in reversing limited T-cell responses or immunological resistance. Thus, a gelatin-tannic acid gel (GelTA) crosslinked bimetallic ($Zn_{0.35}Fe_{0.65}$) magnetocaloric-responsive hydrogels (GelTAMNPs) are developed to mediate pyroptosis-relay-immunotherapy for suppressing post-operation tumor recurrence and metastasis. After surgical resection of tumor, GelTAMNPs generate hyperthermia inducible by alternating magnetic field and release ions (Fe^{3+}, Fe^{2+}, and Zn^{2+}), reinforcing pyroptosis. Subsequently, the cell contents and cytokines released due to pyroptosis act as a "relay baton" passed from the tumor to the lymph nodes, leading to an enhanced systemic immune response. Combined with the PD-1 immune checkpoint blockade, the recurrence and metastasis are significantly suppressed. An in vivo preclinical study on B16F10 tumor-bearing mice demonstrates a long-lasting immunological activation due to post-surgical administration of GelTAMNPs. Altogether, the presented hydrogel exhibits a potential high magnetic sensitive pyroptosis-relay-immunotherapeutic platform for postoperative adjuvant treatment.

1. Introduction

Surgery remains the mainstream therapeutic intervention for managing early-stage cancers.[1] However, a proportion of cancer patients develop recurrence and metastasis even after complete resection of the tumor. It is worth noting that this phenomenon contributes to ≈90% of cancer-related deaths.[2] Several reports have described that disseminated tumor cells[3] or circulating tumor cells[4] can lead to underestimating the true tumor stage macro- and microscopically,[5] thus leading to the dissemination of cancer cells to distant tissues at the time of surgery.[6] Several studies have reported to eliminate those so-called "dormant cells" using different therapeutic strategies[7] involving radiation therapy,[8] chemotherapy,[9] and immunotherapy.[10] Immunotherapy could elicit specific and long-lasting adaptive immune responses to accomplish enduring tumor retreatment.[11] Therefore, a consensus has emerged on the crucial role of immunotherapy in managing metastases.

S. Wang, H. Jing, R. Yang, Y. Zhou, X. Liang, N. Li
Tianjin Key Laboratory of Drug Delivery & High-Efficiency
School of Pharmaceutical Science and Technology
Tianjin University
Tianjin 300072, China
E-mail: linan1985@tju.edu.cn

S. Wang
Department of Surgery
Yong Loo Lin School of Medicine
National University of Singapore
Singapore 119228, Singapore

Z. Heger, S. Krizkova, V. Adam
Department of Chemistry and Biochemistry
Mendel University in Brno
Brno CZ-61300, Czech Republic
E-mail: vojtech.adam@mendelu.cz

The ORCID identification number(s) for the author(s) of this article can be found under https://doi.org/10.1002/adfm.202314194

DOI: 10.1002/adfm.202314194

However, immunotherapy still faces significant challenges, including long-acting immune stimulation impediment[12] and inflammatory irritation after surgery.[13]

Researchers often focus on reshaping the tumor microenvironment (TME)[14] to boost the immune response to balance the complexity between malignant cells and the immune defense system.[15] Emerging evidence has indicated that pyroptosis[16] could reactivate the immune system and enhance tumor immunogenicity. Pyroptosis is driven by a multiprotein complex that can activate proinflammatory caspases, the clusters of proteins associated with apoptosis formation, as well as discharging interleukins (IL), such as IL-18 and IL-1β.[17] The gasdermin-D (GSDMD) protein unveiled by Shao et al. usually remains inhibited in natural conditions.[18] Followed by caspase cleavage, the gasdermin-N domains released from GSDMD bind with membrane phospholipids to perforate cell membranes. Therefore, the osmotic potential is disturbed, resulting in cell swelling and rupture.[19] It must be noted that this phenomenon triggers the release of numerous tumor-associated antigens (cytokines and cell debris) responsible for supporting the activation and maturation of cytotoxic T cells and dendritic cells (DCs).[20]

As a unique subset of regulated cell death, immunogenic apoptosis is characterized by the production of epitopes that bind to antigen-presenting cells via cell perishing. The adaptive immune response is activated by recognizing and phagocytizing dead cells' antigens and presenting them to T cells.[21] Using a "relay baton" passing process, the non-immunogenicity changes to immunogenicity (endogenic immunogenicity of dead tumor cells), thus mediating the body to produce an antitumor immune response.[22]

Hydrogels can be employed to maintain sustainable effects via their in situ tumor bed implanting to achieve a long-lasting and efficient immune response.[23] Gelatin (Gel), a common natural hydrogel, has been frequently investigated due to its low cost, high biocompatibility, and no skin irritation properties. Gel contains arginine-glycine-aspartic acid sequences that exhibit hemostatic activity and promote cell adhesion.[24] Notably, via plentiful hydrogen bonds among the amido-, carboxy- and hydroxy- groups, the Gel can be simply crosslinked with tannic acid (TA),[25] a plant-derived polyphenol possessing intrinsic anti-inflammatory, antioxidant, and antibacterial effects.[26] The resulting gelatin-tannic acid gel (GelTA) hydrogel is a green chemistry natural material rather than a synthetic polymer, thus a promising candidate for application to wounds caused by surgical interventions. The 3D hydrophilic polymeric architecture of the GelTA, resembling an extracellular matrix, could also improve wound healing and tissue regeneration.[27]

Considering the deep localization of residual tissues, achieving a highly penetrating and sustained tumor-killing strategy is of utmost importance. Therefore, in situ, magnetic-responsive hydrogel implantation and external stimulation might be promising strategies for enhancing anticancer efficacy. Magnetic nanomaterials with non-invasively remote actuation, precise temporal and spatial control, and rapid magnetic response could be potential candidates to mediate smart controlling capabilities.[28] Due to their remarkable sensitivity to alternating magnetic fields (AMF), magnetic nanoparticles (MNPs) are essential for formulating hydrogels toward smart regulation of their properties.[29] Iron oxide (Fe_3O_4) nanoparticles acted as the model material in magnetic biomedical engineering for years. However, the use of conventional Fe_3O_4 nanoparticles is limited by their low saturation magnetization (M_s) value, accentuating the non-tunable magnetism problem. Doped metal ferrites, including MFe_2O_4 (M = Zn^{2+}, Mn^{2+}, and Co^{2+}), perform significantly superior to Fe_3O_4 in imaging contrast, ion degradability, and AMF-triggered hyperthermia effects.[30] By switching off AMF, hydrogels could be fabricated to induce various response modes such as deformation, locomotion, and local magnetic hyperthermia (MH), thus killing residual tumor tissue after surgery.

Herein, we crosslinked a bimetallic nanoalloy ($Zn_{0.35}Fe_{0.65}$) Fe_2O_4 with a pure, natural, biodegradable material GelTA to yield a magnetic responsive smart hydrogel (GelTA-($Zn_{0.35}Fe_{0.65}$) Fe_2O_4), hereinafter referred to as GelTAMNPs. Under AMF, the ($Zn_{0.35}Fe_{0.65}$) Fe_2O_4 MNPs inside the gel matrix could generate MH as well as release ions, thus continuously killing tumor cells by inducing pyroptosis. Consequent release of intracellular content, debris, and cytokines (IL-18, IL-1β) caused by pyroptosis acts as the "relay baton" passed from the tumor cells to the lymph nodes, subsequently triggering immunogenic cell death (ICD). Eventually, after antigen presentation by DCs, the activated immune system recruited a large number of T lymphocytes. With the combination of PD-1 checkpoint blockade, an efficient abscopal effect was observed, leading to tumor recurrence and metastasis regression (**Scheme 1**). The presented results demonstrate that GelTAMNPs are promising candidate for postoperative adjuvant therapy that could open new horizons toward advanced immunotherapeutic strategies.

2. Results and Discussion

2.1. Preparation and Characterization of GelTAMNPs

The GelTAMNPs preparation procedure is schematized in **Figures 1A** and S1 (Supporting Information). First, the ($Zn_{0.35}Fe_{0.65}$) Fe_2O_4 MNPs were synthesized. This was achieved by mixing ammonium acetate, $ZnCl_2$, and $FeCl_3$, forming the irregular brown ammine complex $Zn[FeCl_5(NH_3)_x]$. The brown ammine complex turned into a dispersion of regular spherical nanoparticles by chitosan modification. During the solvothermal decomposition, ammonia gas was released from the ammine complex. Thus, the black, porous, hollow spherical MNPs, ($Zn_{0.35}Fe_{0.65}$) Fe_2O_4, were synthesized. An NdFeB magnet was employed to isolate the MNPs. The surface of MNPs contained hydroxyl groups, which were easily adopted as a functional layer for attaching other linkers. Based on that, the hydrophilic GelTA was added to coordinate with MNPs. As soon as the TA-Fe^{3+} complex was synchronized with a hydrogen bond to modify the surface, the yielded product GelTA-($Zn_{0.35}Fe_{0.65}$) Fe_2O_4 became hydrophilic due to crosslinking.

The synthesized ($Zn_{0.35}Fe_{0.65}$) Fe_2O_4 MNPs exhibited remarkable monodispersity (Figure 1B–D) with a well-defined 162.4 ± 35.6 nm diameter. Figure 1E shows the energy-dispersive spectroscopy (EDS) mapping micrographs of ($Zn_{0.35}Fe_{0.65}$) Fe_2O_4 MNPs that confirm homogeneous Fe, O, and Zn distribution within the MNPs. Further, to investigate the chemical state of the ($Zn_{0.35}Fe_{0.65}$) Fe_2O_4 MNPs, X-ray photoelectron spectroscopy (XPS) data were acquired at Zn 2p, Fe 2p, and O 1s (Figure 1F–I). The gathered data validated that the primary Zn components in

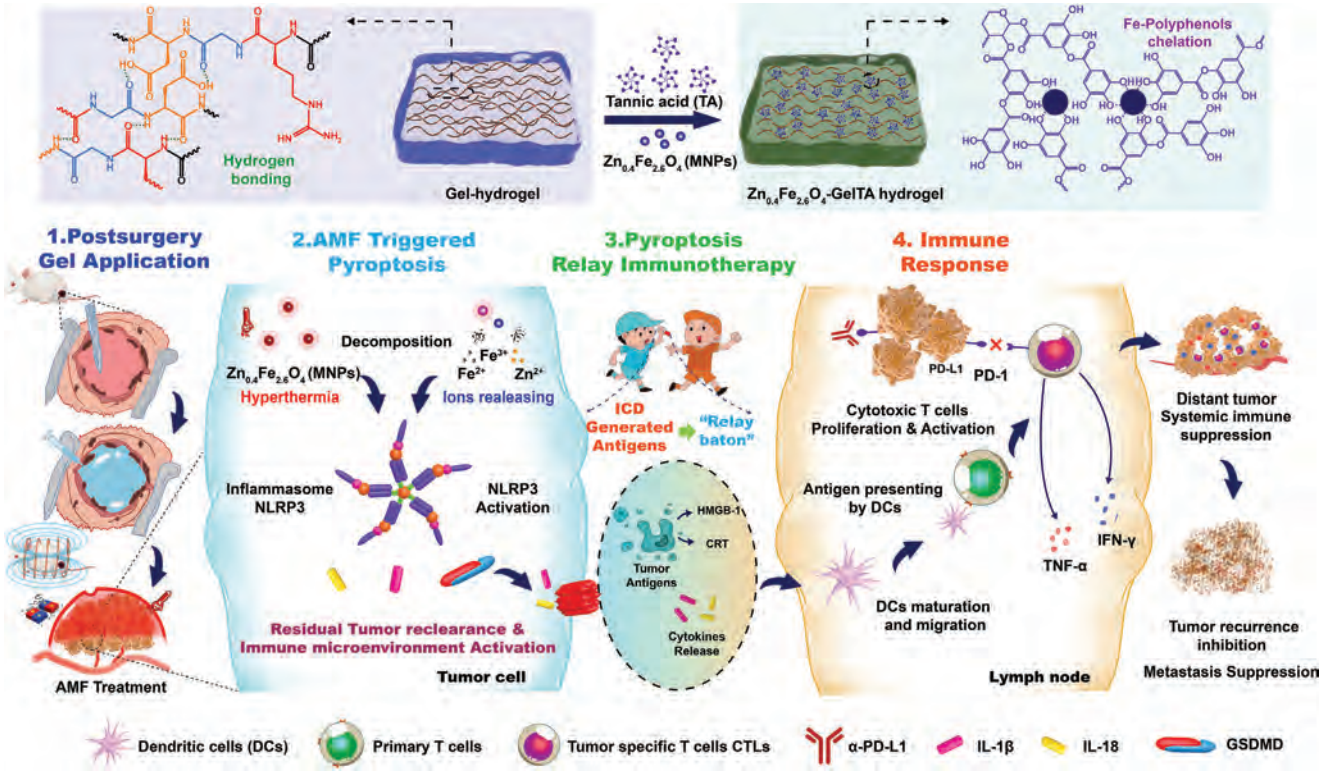

Scheme 1. Mechanism of action and preparation of the $(Zn_{0.35}Fe_{0.65})$ Fe_2O_4 hydrogel-based therapeutic system. The gelatin matrix was crosslinked with tannic acid and designated as GelTA. The GelTA hydrogel conjugated with $(Zn_{0.35}Fe_{0.65})$ Fe_2O_4 is referred to as GelTA-$(Zn_{0.35}Fe_{0.65})$ Fe_2O_4 MNPs (GelTAM) hydrogel. This injectable hydrogel was developed to load magnetic responsive agents to treat recurring neoplasm as well as its metastasis through local implantation.

$(Zn_{0.35}Fe_{0.65})$ Fe_2O_4 MNPs were ZnO: 1021.89 eV and Zn 2p3/2: 1043.59 eV. The predominant valence states for the Fe components were Fe^{2+} (in the 2p3/2 orbit at 709.6 eV) and Fe^{3+} (in the 2p1/2 orbit at 724.8 eV). A superconducting quantum interference device was employed to investigate further the coupled magnetism of the $(Zn_{0.35}Fe_{0.65})$ Fe_2O_4 MNPs. Based on the M–H curve profile of the $(Zn_{0.35}Fe_{0.65})$ Fe_2O_4 MNPs, the Ms value was determined to be 89.5 emu g^{-1} (Figure 1J). Besides, no obvious remanence (Mr) or coercivity (Hc) was observed, suggesting the superparamagnetic character of the $(Zn_{0.35}Fe_{0.65})$ Fe_2O_4 MNPs. The data clearly indicated that the $(Zn_{0.35}Fe_{0.65})$ Fe_2O_4 MNPs were magnetically exchange-coupled. The crystalline phase of the $(Zn_{0.35}Fe_{0.65})$ Fe_2O_4 MNPs was further analyzed by X-ray diffraction (XRD) (Figure 1K). The XRD analyses revealed a series of diffraction peaks at 18.001, 29.601, 34.891, 36.492, 42.306, 52.602, 56.022, 61.385, 72.749, and 73.709 that could be well indexed to (111), (220), (311), (222), (004), (422), (511), (440), (533), and (622) plane of spinel $(Zn_{0.35}Fe_{0.65})$ Fe_2O_4 (PDF#19-0629). The hydrogel was analyzed using Raman spectroscopy after gelation at 4 °C and GelTAMNPs formation. As shown in Figure 1L, the GelTAMNPs spectra contained amplified peaks at 450, 624, and 976 cm^{-1}, which indicated the chelation of GelTA-$(Zn_{0.35}Fe_{0.65})$ Fe_2O_4 MNPs. Further, the Fourier-transformed infrared spectroscopy (FT-IR) analysis revealed a shift in intermolecular hydrogen bonding from 2928 to 3437 cm^{-1}, along with a strengthening of the C–N stretch in amide at 1419–1444 cm^{-1}. These findings suggest that TA and GelTA formed the coating layer on the $(Zn_{0.35}Fe_{0.65})$ Fe_2O_4 MNPs (Figure 1M). Scanning electron microscope examinations conclusively verified the even dispersion of GelTA and GelTAMNPs, signifying the successful amalgamation (Figure S1, Supporting Information). In addition, the gelation process of Gel, GelTA, and GelTAMNPs is presented in Figure S2 (Supporting Information). The stability of GelTAMNPs in different solutions could be affirmed via dynamic light scattering (DLS) investigation (Figure S3, Supporting Information). Based on the data, it could be concluded that the progress of gelation is proportional to the concentration. The highest gelling efficiency was achieved when the concentration reached 20 *w/v*.

2.2. Dynamic Mechanical Analysis and Ion Release of GelTAMNPs

As can be seen from **Figure** 2A, the hydrogel containing only Gel appeared transparent yellow. As TA was added and crosslinked with Gel, the hydrogel exhibited a white flocculent appearance. Further, when the $(Zn_{0.35}Fe_{0.65})$ Fe_2O_4 MNPs were added to the hydrogel, it turned gradually darker, correlating with the increasing amount of added $(Zn_{0.35}Fe_{0.65})$ Fe_2O_4 MNPs (from 1× to 3×). Additionally, dynamic mechanical analysis (DMA) at a strain range of −120 to 0% was utilized to clarify the mechanism of the gelling process of GelTAMNPs (Figure 2B–F). The storage (E′) and loss (E″) moduli values remained consistently stable within the analyzed strain range. Doping with $(Zn_{0.35}Fe_{0.65})$

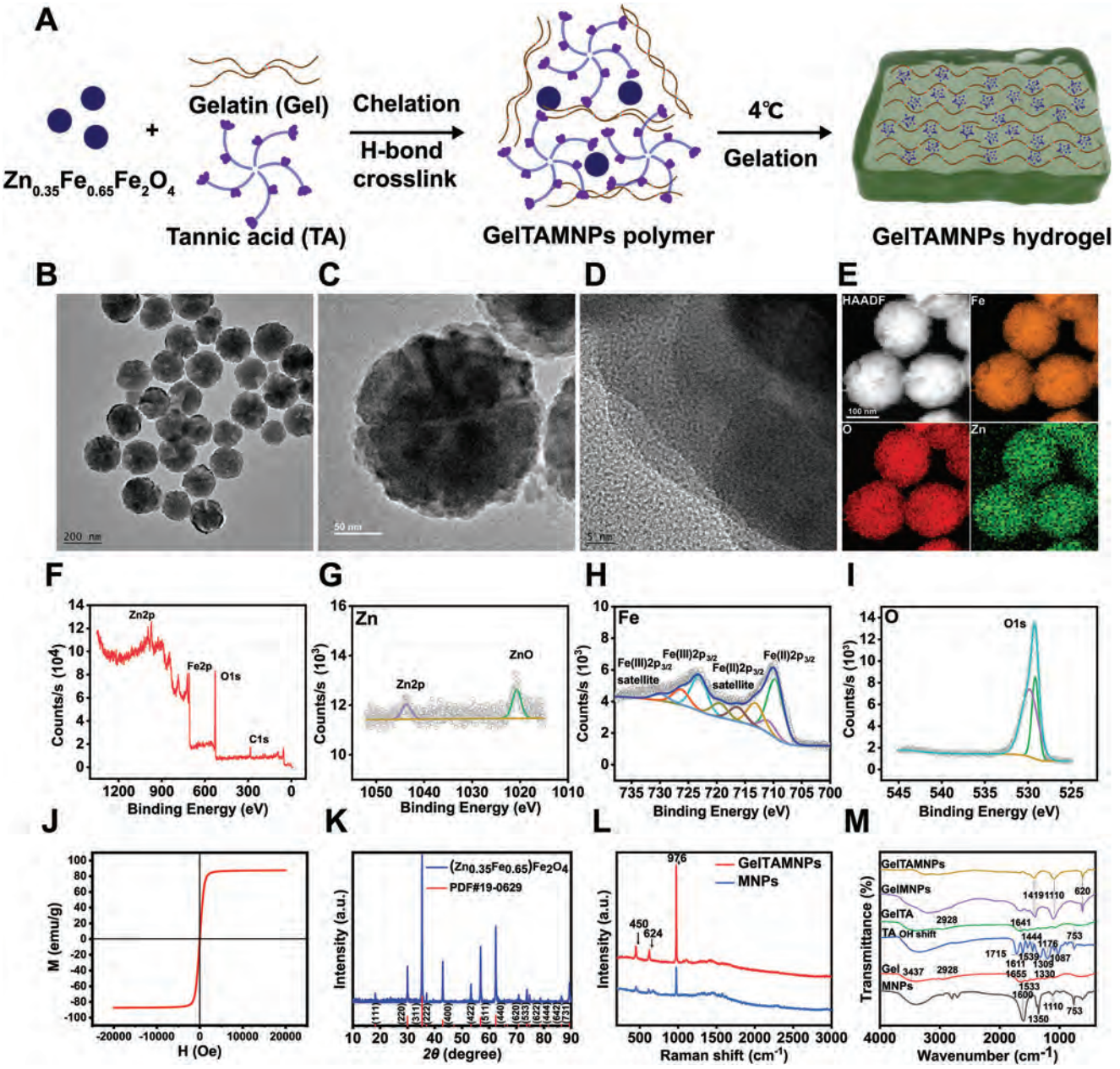

Figure 1. Characterization of the physicochemical properties of $(Zn_{0.35}Fe_{0.65})$ Fe_2O_4 MNPs and GelTAMNPs. A) Schematic illustration of the formation of GelTAMNPs hydrogel. B–D) TEM micrographs of $(Zn_{0.35}Fe_{0.65})$ Fe_2O_4 MNPs at different magnifications. E) EDS mapping of $(Zn_{0.35}Fe_{0.65})$ Fe_2O_4 MNPs. F) XPS survey of $(Zn_{0.35}Fe_{0.65})$ Fe_2O_4 MNPs. XPS analysis of G) Zn, H) Fe, and I) O. J) H–M loop analysis of $(Zn_{0.35}Fe_{0.65})$ Fe_2O_4 MNPs. K) XRD spectrum of $(Zn_{0.35}Fe_{0.65})$ Fe_2O_4 MNPs. L) Raman spectra of $(Zn_{0.35}Fe_{0.65})$ Fe_2O_4 MNPs and the formulated GelTAMNPs hydrogel. M) FT-IR spectra of individual components of GelTAMNPs and the formulated hydrogel.

Fe_2O_4 MNPs caused the E′and E″ values to change significantly from −60% to −80%, revealing that MNPs improved the straining tolerance of GelTAMNPs. Figure 2G illustrates the photodocumentation of GelTAMNPs degradation. The GelTAMNPs initially appeared as a black, lumpy solid that dissociated over time to a discrete purple cloud-like state due to the formation of the purple tannic acid-iron coordination compound from the iron ions released from the dissociated $(Zn_{0.35}Fe_{0.65})$ Fe_2O_4 MNPs and the TA in the GelTA matrix. In contrast, non-doped GelTA degraded to a pale-yellow cloudy state without any purple coloration.

Inductively coupled plasma mass spectrometry (ICP-MS) was employed to evaluate the degradation of hydrogels and the subsequent release of ions from GelTAMNPs. The standard curves of Fe (Figure 2H) and Zn (Figure 2I) were first constructed using standard internal reference testing. Then, the GelTAMNPs were stored at various pH levels (4.5, 5.5, and 7.4) for 16 days to quantify the release of Fe and Zn ions. Based on the cumulative

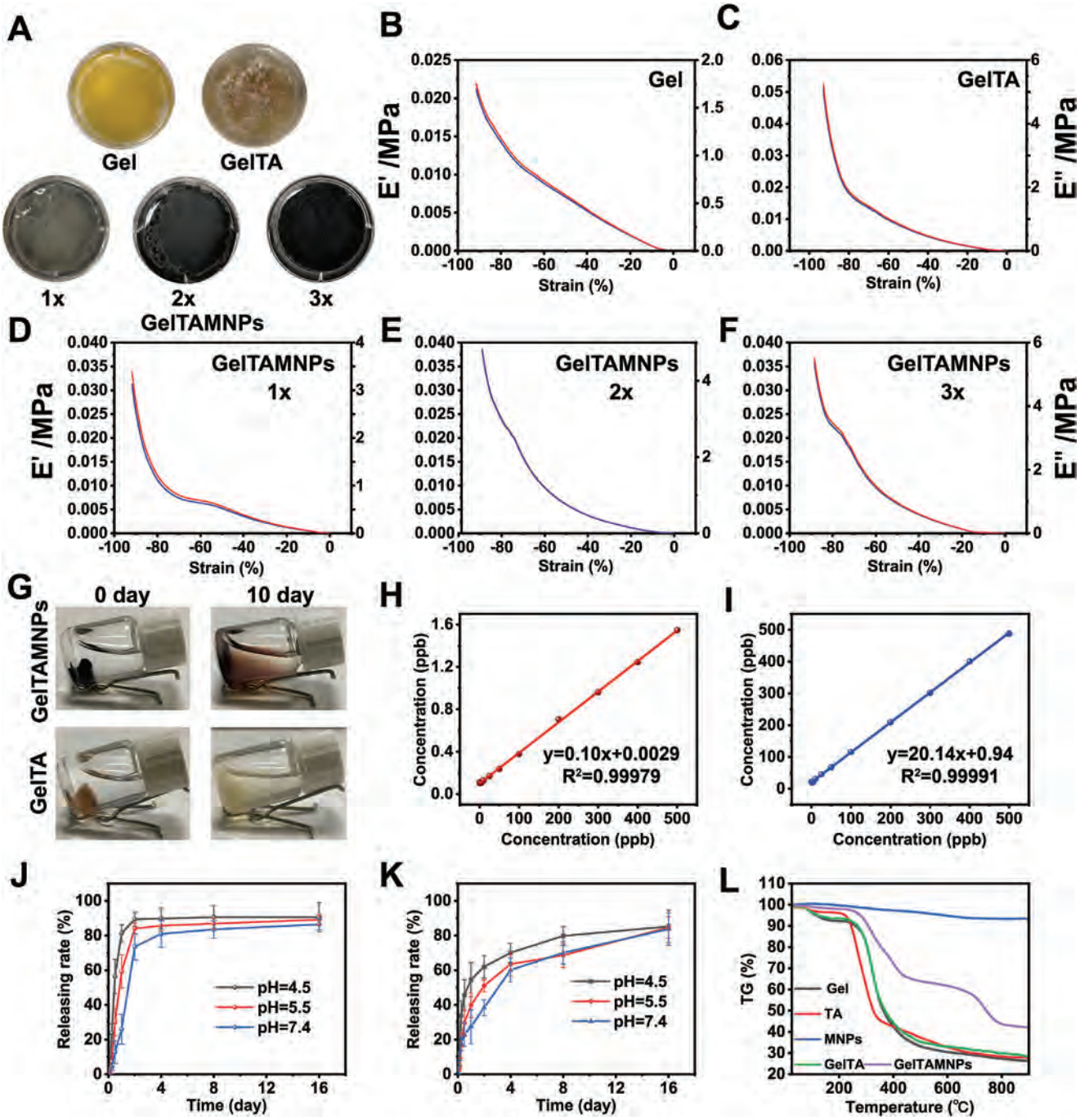

Figure 2. Characterization of properties of the GelTAMNPs hydrogel. A) Digital photographies of hydrogels containing only Gel, GelTA, and GelTAMNPs doped with different amounts of ($Zn_{0.35}Fe_{0.65}$) Fe_2O_4 MNPs [1× (20 mg), 2× (40 mg), and 3× (60 mg)]. DMA analysis of B) Gel, C) GelTA, D) GelTAMNPs (1×), E) GelTAMNPs (2×) and F) GelTAMNPs (3×). G) Digital photodocumentation of degradation of GelTAMNPs (*upper photos*) and GelTA (*lower photos*). H) Standard curve of Fe analysis by ICP-MS. I) Standard curve of Zn analysis by ICP-Ms. Cumulative release of J) Fe and K) Zn from GelTAMNPs at different pH values (7.4, 5.5, and 4.5). L) TGA of individual components of GelTAMNPs and the formulated GelTAMNPs.

release curves, it can be stated that a lower pH (4.5) could accelerate the release of both the analyzed ions. The release profiles demonstrated that after 8 days, 80% of Fe and Zn ions were released from GelTAMNPs (Figure 2K), confirming the observed degradation process shown in Figure 2G.

Thermogravimetric analyses (TGA) revealed that the Gel underwent 81.7% degradation at 850 °C (Figure 2L). Furthermore, it exhibited a gradual breakdown of TA at temperatures exceeding 200 °C, which commenced a decarboxylation. Gel, TA, and GelTA exhibited a second stage of weight loss, occurring approximately

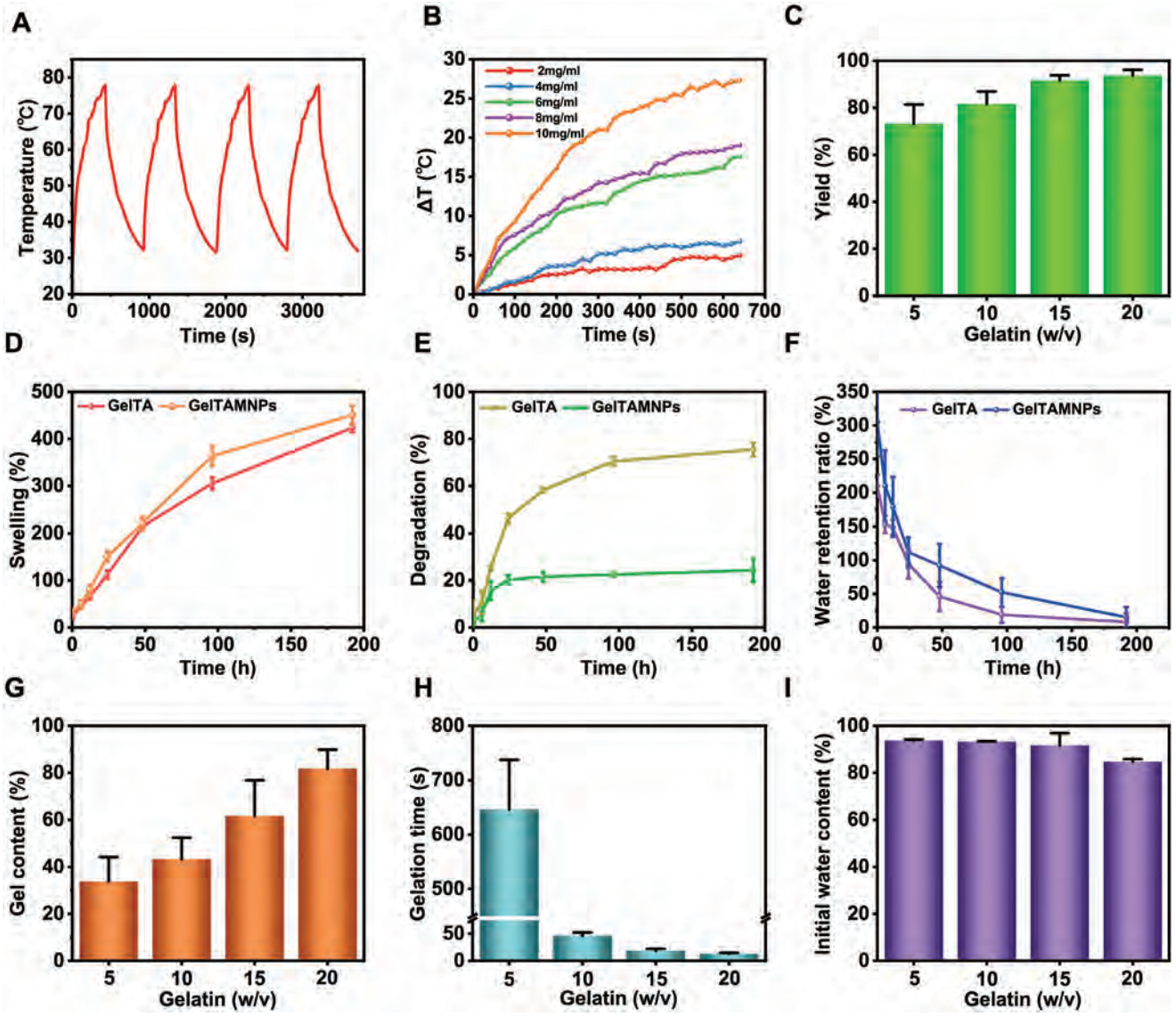

Figure 3. Physicochemical properties of the GelTA and GelTAMNPs hydrogels. A) Temperature elevation cycles of MNPs under AMF. B) Temperature curves of various concentrations of MNPs under AMF. C) Yield of hydrogelation of GelTAMNPs. D) Percentage of swelling, E) Tendency of degradation, and F) Water retention ratio of the GelTA and GelTAMNPs hydrogels. G) Gel content related to the Gel amount used for GelTAMNPs formulation. H) Relation between Gel amount and gelation time, and I) IWC of GelTAMNPs.

between 200 and 600 °C, attributed to the thermal breakdown of both main and side structures. In addition, due to the high hydrophilicity of the analyzed materials, these hygroscopic components exhibited a propensity for absorbing moisture from the atmosphere, leading to stepwise decomposition. In contrast, for $(Zn_{0.35}Fe_{0.65})$ Fe_2O_4 MNPs, no noticeable weight loss was observed during the heating process. Additionally, the remaining weight was over 29.37% in GelTAMNPs, compared with free Gel (26.70%) and TA (27.98%). This can be plausibly attributed to the hydrogen bonding between TA and Gel, which limited the mobility of chains, enhancing thermal stability. This observation is supported by derivative thermogravimetric data, evidenced by the lower rate of maximum degradation for GelTAMNPs (0.5%/°C) compared to pure Gel (0.6%/°C) and TA (0.7%/°C) (Figure S4, Supporting Information). Altogether, the alternations of GelTAMNPs are owing to the chelation between metals and GelTA matrix ligands.

2.3. Hyperthermia Studies, Swelling, Degradation, and Water Retention of GelTAMNPs

In the next step, the stability of magnetic-thermal conversion in GelTAMNPs was examined. While subjected to AMF, the recorded temperature increased to between 78 and 80 °C (**Figure** 3A). Comparable results were achieved by recording and analyzing the thermal images (Figure S5, Supporting Information). The solid state of GelTAMNPs could be melted to liquid

under AMF. At the same time, the liquefied gel could fill the gaps between the silicon spheres (Figure S6, Supporting Information), thus proving its potential application in wound filling after surgery. The experiments demonstrated the reliability and controllability of GelTAMNPs, as no apparent MH efficacy loss was observed during the cycles. Magnetic hyperthermia properties of GelTAMNPs were further evaluated using various concentrations of $(Zn_{0.35}Fe_{0.65})$ Fe_2O_4 MNPs (2, 4, 6, 8, and 10 mg mL^{-1}) in the GelTAMNPs (Figure 3B). The data confirmed that the magnetothermal effect was markedly boosted with increasing amounts of doped $(Zn_{0.35}Fe_{0.65})$ Fe_2O_4 MNPs. Interestingly, with the highest amount of MNPs (10 mg mL^{-1}) in the GelTAMNPs, 28 °C was the highest ΔT, confirming $(Zn_{0.35}Fe_{0.65})$ Fe_2O_4 as an ideal dopant for follow-up therapeutic experiments involving induced hyperthermia. The yield of hydrogelation was ascertained to be strictly concentration-dependent. When the gelatin concentration reached 20 *w/v*, the yield of hydrogelation of GelTAMNPs was ≈91.5% (Figure 3C). The initial water content (IWC) and porosity of GelTA and GelTAMNPs are depicted in Figure S7 (Supporting information). These properties markedly declined for GelTAMNPs compared with GelTA. This could be plausibly explained by the fact that adding MNPs filled the space of the net linking structure of GelTA. Comparing the G´ and G″ values of GelTAMNPs, GelTA, and Gel, it can be observed that the structural integrity was enhanced with the addition of MNPs, thus facilitating the scope of potential bioapplications (Figure S8, Supporting Information).

Hydrogels are generally characterized by an array of unique features, including water retention, swelling, and degradation rate. Swelling, regarded as one of the pivotal characteristics, significantly influences substance encapsulation and wound exudate absorption. In general, the elevated osmolarity, as well as the hydrophilic gel network, results in water uptake and hydrogel swelling. In GelTA and GelTAMNPs, after 50 h, the swelling rate was ≈200%. In comparison, more than 400% of swelling was determined after 200 h (Figure 3D), indicating the physical crosslinking between TA and Gel that creates stable hydrogels. Due to the reduced hydrogen bonding and the unbound branches of GelTAMNPs, the degradation rate reached 80% after 96 h, twofold higher than that observed for GelTA (Figure 3E). Evaporation speed is crucial for retaining water within the hydrogel network. In our experiments, water content decreased over time; there was lower water retention in the case of GelTA, and the doping with $(Zn_{0.35}Fe_{0.65})$ Fe_2O_4 MNPs caused nearly 50% delay in water evaporation at 50 h time point (Figure 3F). The Gel content is closely connected with Gel concentration (*w/v*). At 20 *w/v* concentration, the Gel content reached 80% (Figure 3G). In contrast, as the concentration of Gel increased, the gelation time decreased significantly (Figure 3H). Notably, the Gel concentration minimally affected the initial water retention rate (Figure 3I). This data confirmed that GelTAMNPs exhibit advantageous properties for application on post-surgery wounds.

2.4. Examination of Biological Properties of GelTAMNPs In Vitro

The cellular uptake of nanomaterials is closely linked with endolysosomal organelles. Therefore, we next proceeded with additional analysis to assess the colocalization. As demonstrated in **Figure** 4A, GelTAMNPs-administered cells displayed a bright green fluorescence signal, which confirmed that GelTAMNPs were effectively untaken by B16F10 melanoma cells.

Further, GelTAMNPs were incubated with red blood cells (RBCs) to demonstrate their hemocompatibility. As shown in Figure 4B, hemolysis could not be observed even with increasing concentrations of GelTAMNPs. Notably, the hemolysis rate determined for GelTAMNPs (200 μg mL^{-1}) was <5%, suggesting that GelTAMNPs are fully hemocompatible.

The effect of GelTAMNPs on the viability of B16F10 cells was further assayed with and without exposure to AMF (Figure 4C). A high viability (≈80% for the highest applied concentration) was detected in GelTAMNP-exposed cells without AMF. In contrast, exposure to AMF decreased the viability (≈60%) of the B16F10 cells (Figure 4C). The relative IC50 values of GelTAMNPs with or without AMF were 723.4 and 1309 μg mL^{-1}, respectively (Figure S9, Supporting Information). This confirmed that GelTAMNPs exhibit ideal biocompatibility for AMF-triggered antitumor therapy.

2.5. Evaluation of Cell Death Types Induced by GelTAMNPs

Initially, the cell morphological changes were analyzed by bright-field microscopy; dying cells could be clearly identified due to the swelling and rupture of the plasma membrane (Figure S10, Supporting Information). Next, we conducted the flow cytometric investigation to gain additional understanding regarding the B16F10 killing ability of GelTAMNPs with AMF (Figure 4D,E). As demonstrated, few to no dead cells were detected in the phosphate-buffered saline (PBS) group. In addition, a relatively small number of dead cells was discovered in the GelTAMNPs group without AMF. In contrast, AMF exposure resulted in substantial induction of >20% cell death. Finally, we also examined the possible induction of pyroptosis through Western blotting of GSDMD, GSDME, and NLRP3. The obtained data (Figure 4F,G; Figure S11, Supporting Information) demonstrated that the highest expression of the pyroptosis markers was in cells treated with GelTAMNPs exposed to AMF, suggesting that the proposed therapeutic strategy utilizing GelTAMNPs and AMF also activated pyroptosis.

2.6. Preparation and Characterization of GelTAMNPs

Next, we focused on examining the anti-migratory properties of GelTAMNPs using a wound-healing assay (**Figure** 5A). The quantification (Figure 5C,D) of wound width revealed that control B16F10 cells exhibited strong and aggressive motility and were able to close an artificial wound in 24 h nearly. In contrast, administration with GelTAMNPs followed by AMF exposure significantly inhibited cell migration even after 12 to 24 h. The cells were able to close 8.41 and 7.81% of the artificial wound after 12 and 24 h, respectively. After that, we continued analyzing the anti-invasiveness properties of GelTAMNPs hydrogel. For this purpose, a transwell migration assay was performed to assess the invasion and migration abilities of B16F10 cells after a 24-hour

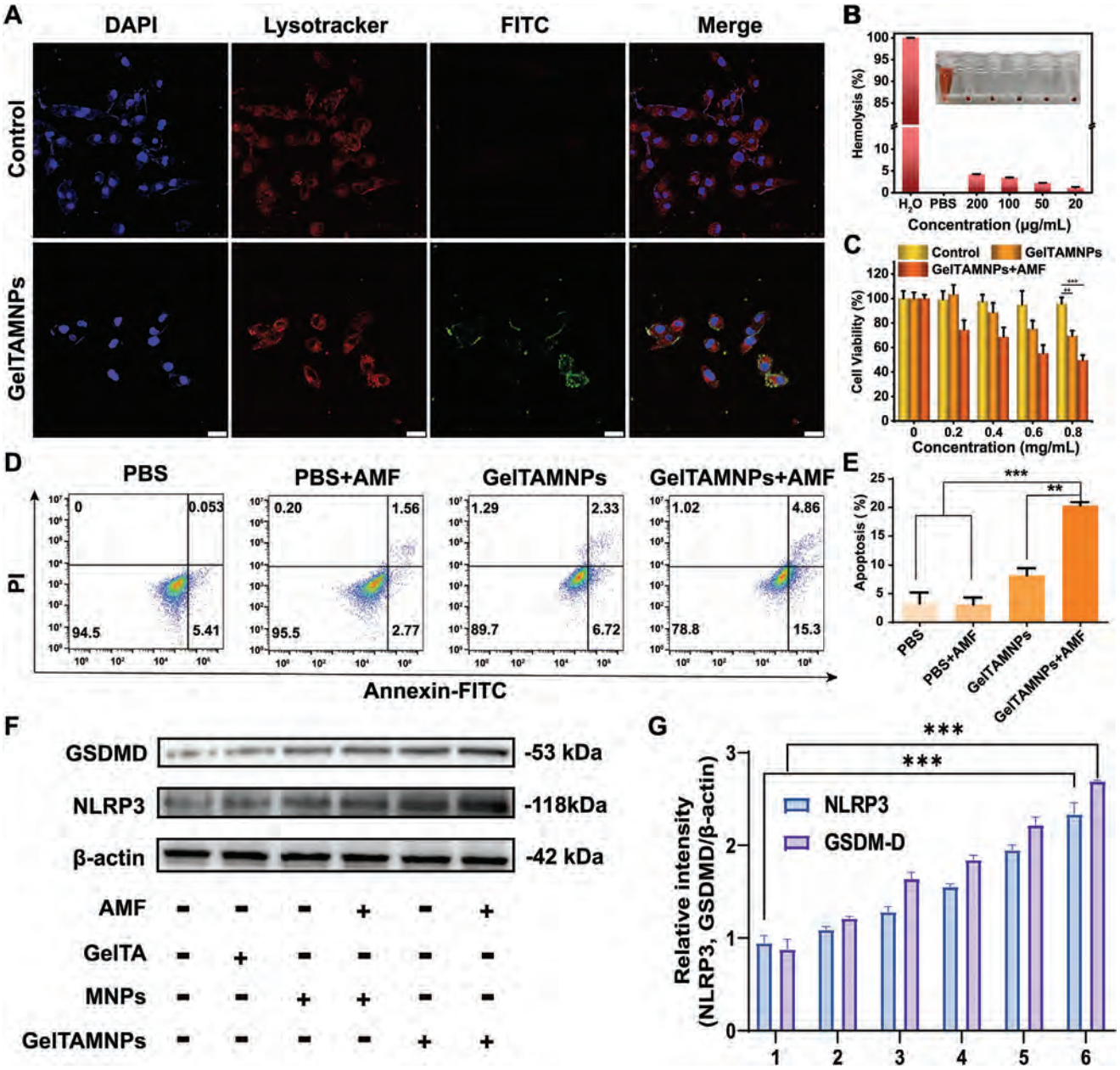

Figure 4. Interactions between GelTAMNPs and B16F10 cells in vitro. A) Cellular uptake of B16F10 cells administered with PBS (control) and FITC-labeled GelTAMNPs. Scale bar: 10 μm. B) Hemolysis was evaluated as hemoglobin release from RBCs incubated with GelTAMNPs, PBS (negative control), or H_2O (positive control). C) Analysis of the viability of B16F10 cells administered to GelTAMNPs with or without exposure to AMF. D) Flow cytometry dot plots showing B16F10 cells treated with PBS (negative control) and GelTAMNPs with or without AMF and stained using FITC-Annexin/PI. E) Quantitation of apoptotic cells analyzed by flow cytometry. F) Western blotting of proteins involved in pyroptosis; β-actin, loading control. G) Densitometric analysis of western blots carried out using ImageJ software: 1, PBS; 2, GelTA; 3, MNPs; 4, MNPs + AMF; 5, GelTAMNPs; and 6, GelTAMNPs + AMF. The data are expressed as mean ± SD, $n = 3$, $^{*}p < 0.05$, $^{**}p < 0.01$, and $^{***}p < 0.001$.

treatment. As shown in Figure 5B,E, only 11.5% of cells treated with GelTAMNPs and exposed to AMF successfully migrated to the lower chamber; in contrast, the control cells treated with PBS had a migration rate of 98.7%. Therefore, it can be concluded that GelTAMNPs combined with AMF exposure significantly inhibit migration and invasiveness of B16F10 cells; hence, it is a suitable candidate for follow-up in vivo experiments.

2.7. Multimodal In Vivo Imaging

Mice bearing B16F10 tumors were administered GelTAMNPs or saline via intratumoral injection to conduct in vivo imaging. Subsequently, the mice were exposed to 6.6 kW, 40 kA m^{-1}, 309 kHz AMF for 90 s. As depicted in **Figure** 6A, the tumor site temperature of the GelTAMNPs administered mice increased to 60.9 °C.

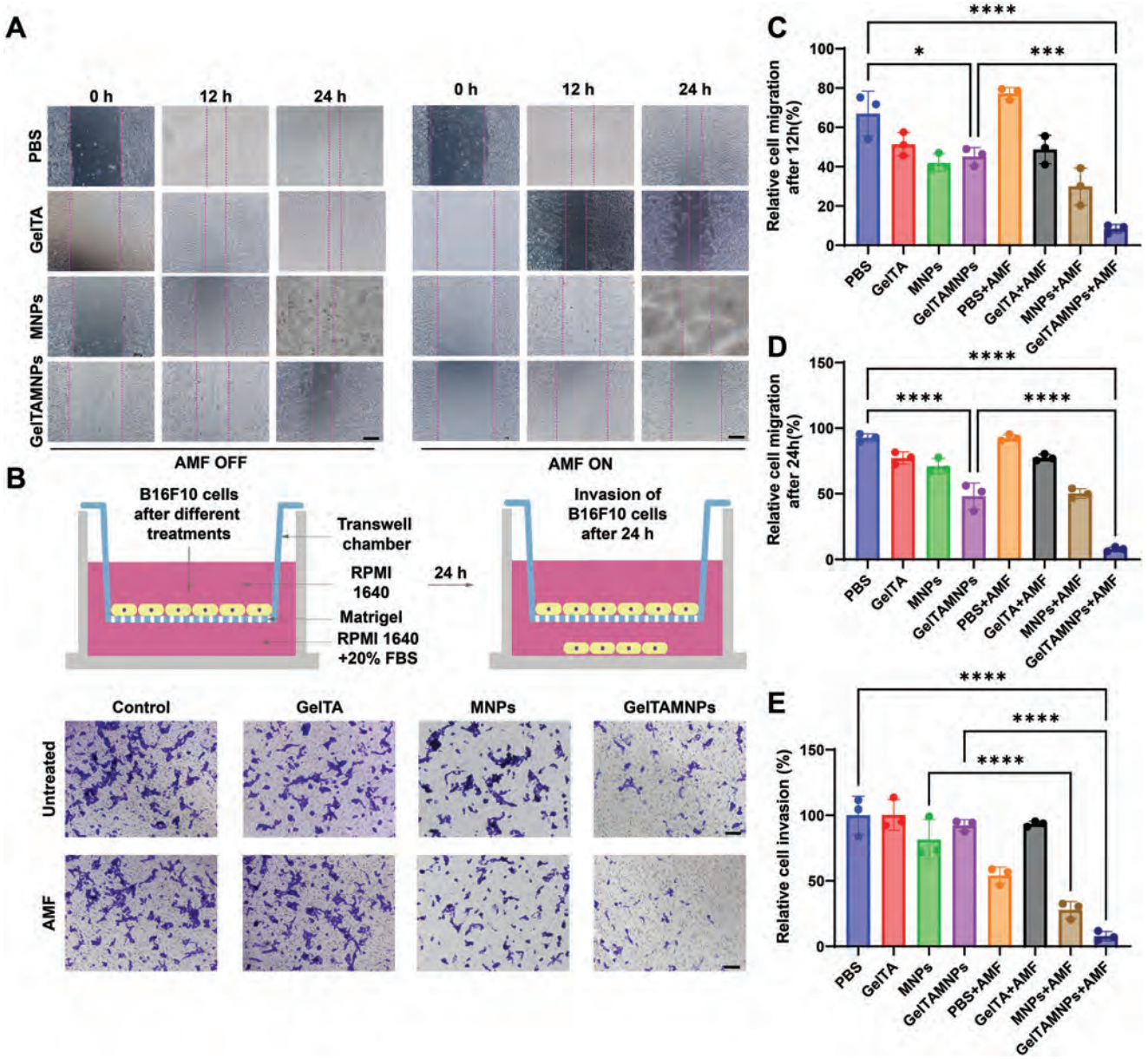

Figure 5. Evaluation of anti-migratory and anti-invasiveness properties of GelTAMNPs in vitro. A) Representative micrographs of wound-healing assay of B16F10 cells administered with annotated treatments captured at 0, 12, and 24 h time points. Scale bar, 100 μm. B) Schematic depiction of the transwell assay and representative micrographs of B16F10 cells incubated with PBS, GelTA, MNPs, and GelTAMNPs with or without AMF for 24 h. Scale bar, 100 μm. C,D) Quantitation of the cells' ability to enclose the artificial gap after 12 and 24 h incubation. E) Quantitation of relative cell invasion rates after 24 h. Data are expressed as means ± SD ($n = 3$). Statistical significances were calculated via the Student's *t*-test. $^{*}p < 0.05$, $^{**}p < 0.01$, and $^{***}p < 0.001$.

This can be attributed to the GelTAMNPs' exceptional efficiency in converting magnetic energy into hyperthermia (Figure 6B).

Computed tomography (CT) can generate accurate and viable illustrations with remarkable resolution. Therefore, we further determined the possibility of using GelTAMNPs for CT imaging. As shown in Figure 6C, a strong contrast signal at the tumor site was noted at 4 h, validating its CT imaging capability. Compared with the Iohexol group, the signal of GelTAMNPs could be found after over two weeks, which further proved its exceptional properties. By constructing the standard curve of CT values (HU) against concentrations, both GelTAMNPs and Iohexol were discovered to exhibit a strong linear correlation with the R^2 values of 0.99098 and 0.98807, respectively (Figure 6D,E).

2.8. GelTAMNPs for Post-Surgical Treatment of Residual Tumors In Vivo

In this step, we further investigated the anticancer efficacy of GelTAMNPs. We also assessed the significance of AMF exposure in activating its biological effects in vivo. As shown in **Figure** 7A, the animals were divided into the

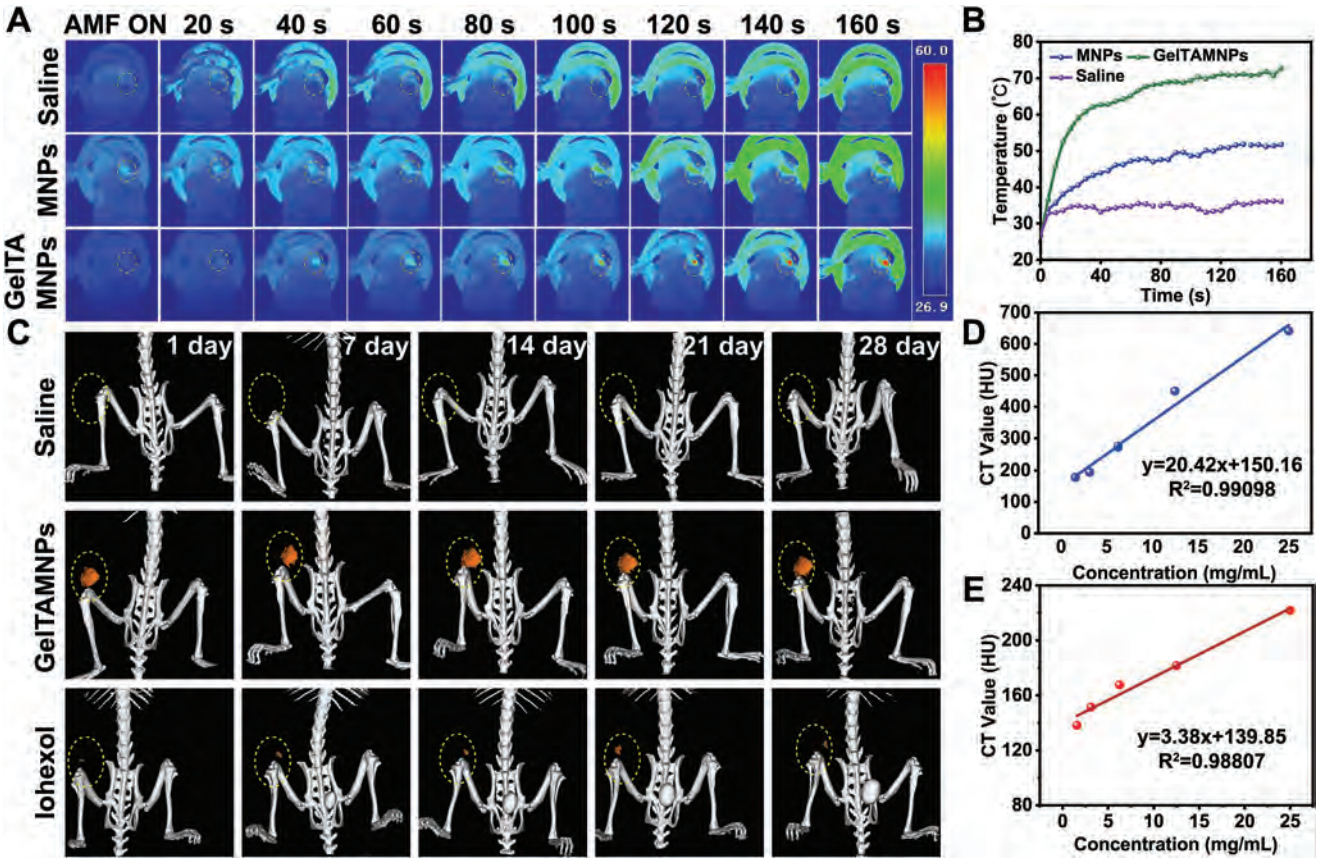

Figure 6. In vivo multimodal imaging performance. A) Real-time thermal images of mice bearing B16F10 tumors after intratumoral saline administration, ($Zn_{0.35}Fe_{0.65}$) Fe_2O_4 MNPs or GelTAMNPs continuously exposed to AMF (up to 160 s). B) Thermal profiles recorded at the tumor sites. C) CT images of mice bearing B16F10 tumors administered with saline, Iohexol, and GelTAMNPs. Standard curves constructed from CT values for D) GelTAMNPs and E) Iohexol.

following groups for experiments—G1: Control, G2: Surgery, G3: Surgery + GelTA, G4: Surgery + GelTAMNPs, G5: Surgery + PD-1, G6: Surgery + GelTAMNPs + AMF, and G7: Surgery + GelTAMNPs + AMF + PD-1. At the experimental endpoint, animals were euthanized, and the main organs and tumor tissue were collected for subsequent experiments. As shown in Figure 7B,C, TUNEL, and hematoxylin-eosin (H&E), staining revealed that the tumors exhibiting the highest amounts of apoptotic cells were those receiving surgery, followed by GelTAMNPs + AMF and PD-1 administration. This finding confirmed the suitability of GelTAMNPs for an advanced combination therapy. To investigate the GelTAMNPs-mediated ICD effect, we analyzed the expression of ICD markers (HMGB-1 and CRT; Figure 7D,E). As immunostaining of excised tumors revealed, the mice treated with the GelTAMNPs + PD-1 and AMF post-surgically exhibited much higher HMGB-1 and CRT expressions than the other groups, suggesting ongoing ICD. The LDH release and ATP secretion (Figure S12, Supporting Information) results further determined the activation of antitumor immunity. Subsequent analyses of mice body weights (Figure S13, Supporting Information) and tumor volumes (Figure 7F; Figure S14, Supporting Information) confirmed that surgery + GelTAMNPs + AMF + PD-1 combination exhibited the highest therapeutic potential and promising biocompatibility with negligible side effects as body weights trends were comparable with controls. Notably, the obtained data demonstrate that the mice in the control group rapidly developed tumors, and the surgery combined with GelTA, GelTAMNPs, or PD-1 groups experienced some extent of tumor growth inhibition; however, after the primary tumor removal, there was recurrence in all cases. This phenomenon was, however, suppressed by combination therapy involving surgery + GelTAMNPs + PD-1 + AMF, which caused 90% inhibition of tumor volumes with significant inhibitory effects on recurrence. Moreover, the group post-surgically treated with GelTAMNPs + PD-1 and AMF exhibited significantly prolonged survival: a median survival of 45 days (Figure 7G). Further, the expression of ILs was analyzed to understand the mechanisms underlying the treatments' therapeutic effects. The obtained data revealed IL-18 and IL-1β secretions in GelTAMNPs-exposed groups (Figure S15, Supporting Information). Finally, the serum AST, CREA-S, ALT, ALB, ALP, UA, TP, and UREA analyses (Figure S16, Supporting Information) confirmed there was no significant undesired organ damage caused by GelTAMNPs, validating its exceptional biocompatibility.

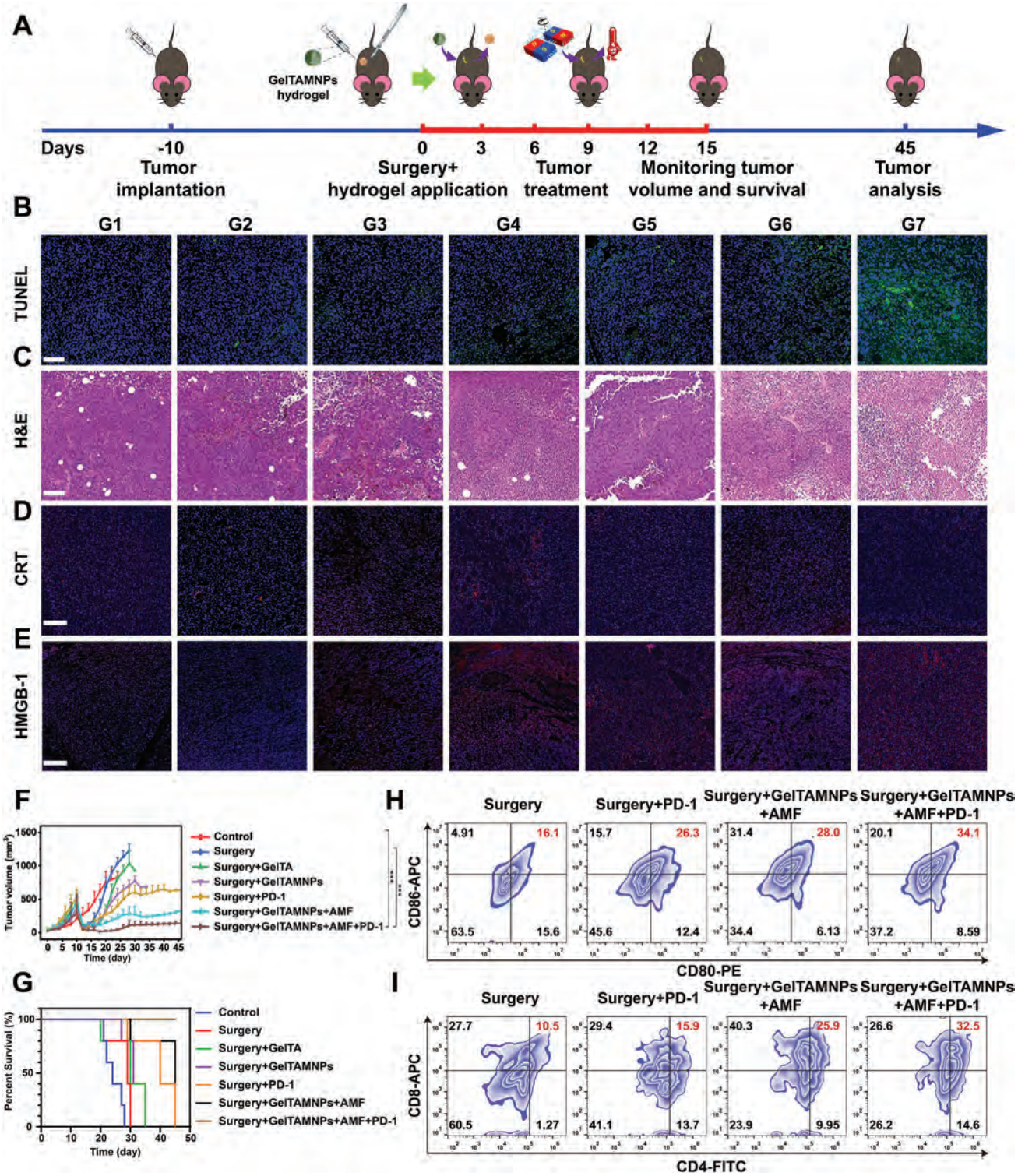

Figure 7. Post-surgical treatment of residual tumor using GelTAMNPs. A) Schematic depiction of the tumor induction process followed by surgery and GelTAMNPs application to the wound. At the experimental endpoint, excised tumors were stained using B) TUNEL and C) H&E. Scale bars, 100 µm. D,E) Immunofluorescence analysis of expression of CRT and HMGB-1 in the tumor tissue; Scale bars, 100 µm. (G1: control, G2: surgery, G3: surgery + GelTA, G4: surgery + GelTAMNPs, G5: surgery + PD-1, G6: surgery + GelTAMNPs + AMF, and G7: surgery + GelTAMNPs + AMF + PD-1, $n = 3$). F) Analysis of tumor volume variation from annotated treatments; ($n = 5$) G) Survival curves of mice receiving annotated treatments; ($n = 5$). H) Typical flow cytometry of mature DCs ($CD11c^+CD80^+CD86^+$) in tumor tissue after stimulation with different treatments ($n = 3$). I) Typical flow cytometry of infiltrated T cells in ($CD3^+CD8^+CD4^+$) in lymphocytes after stimulation with different treatments; ($n = 3$). Statistical significances were calculated via the Student's *t*-test. $^*p < 0.05$, $^{**}p < 0.01$, and $^{***}p < 0.001$.

2.9. Investigating DC Maturation and T Cell Infiltration

Moreover, to gain detailed insights into the molecular mechanisms of GelTAMNPs-based therapy, we further proceeded to stain DCs in tumor tissue to label $CD11c^+$, $CD80^+$, and $CD86^+$ that enabled analyzing DC maturation by flow cytometry (Figure S17, Supporting Information; Figure 7H). Specifically, the DC percentage in the GelTAMNPs + AMF group increased to 34.1% compared with the surgery group (16.1%), demonstrating that GelTAMNPs-mediated treatment could promote DC maturation and induce an efficient immune response. We further analyzed by labeling $CD4^+$, $CD3^+$, and $CD8^+$ to conduct T-cell infiltration (Figure S18, Supporting Information; Figure 7I). The quantitative data among different test groups has been illustrated in Figure S19, Supporting information. The collective average percentages of effector T cells within the combined treatment group were notably greater than those in the single intervention groups (10.5% versus 15.9% and 25.9% versus 32.5%, respectively), indicating that GelTAMNPs + AMF treatment-induced tumor-specific T-cell infiltration. The GelTAMNPs + AMF + PD-1 treatment group exhibited the highest percentage of effector T cells, presenting a threefold increase compared with the surgery group.

2.10. Evaluating the Inhibitory Effects of GelTAMNPs on Distant Tumors and Pulmonary Metastases

In follow-up experiments, we sequentially implanted B16F10 tumors at two different sites in both flanks to evaluate the post-surgically administered GelTAMNPs' ability to inhibit the growth of distant, untreated tumors (schematically depicted in **Figure** 8A). As presented in Figure 8B, the distant tumors were significantly shrunk in the surgery + GelTAMNPs + AMF + PD-1 group mice, suggesting that GelTAMNPs have desired abscopal antitumor activity. To verify the in vivo biostability of GelTAMNPs, a Rhodamine B (RhB)-labeled GelTAMNPs was prepared and employed for the fluorescence imaging of the GelTAMNPs-administered mice for up to 17 days (Figure 8C). The fluorescent intensity analysis (Figure S20, Supporting Information) underscores the enduring robustness of the RhB-labeled GelTAMNPs. The persistent GelTAMNPs fluorescence signal throughout the experimental duration affirms the remarkable biostability of GelTAMNPs, extending beyond an impressive 17 days. The anti-metastatic effects elicited by GelTAMNPs were further investigated during a 21-day treatment regime. At the experimental endpoint (day 21), mice were euthanized, and both the tumors and lungs were gathered to examine the extent of tumor metastasis in vivo (schematically depicted in Figure 8D). Subsequent immunostaining of tumor tissues for evaluating the expression of the proliferation marker Ki-67 revealed extensive positivity without treatments and surgery, GelTA, or GelTAMNPs without AMF exposure. In contrast, the tumors excised from animals from the group that received the combination therapy of surgery followed by GelTAMNPs, PD-1, and AMF exhibited a rather negative Ki-67 staining; this suggests the treatment has efficient anti-proliferative and anti-metastatic properties (Figure 8E). Finally, Bouin's solution was utilized to stain and quantify the amount of pulmonary metastatic nodules (Figure 8F,G). It was ascertained that compared to the groups receiving surgery combined with GelTA or GelTAMNPs without AMF, the groups that received surgery with post-surgical administration of anti-PD-1 and GelTAMNPs followed by AMF exposure exhibited markedly lower numbers of metastatic nodules. Significantly, this phenomenon was most prominent for the group treated with complete post-surgical combination therapy containing GelTAMNPs + PD-1 + AMF. Therefore, it can be stated that the presented data confirmed that this post-surgical combination therapeutic intervention is highly effective in inhibiting the metastatic spread of B16F10 cells to the lungs.

3. Conclusion

In summary, we engineered a bimetallic magnetic nanoarchitectonics $(Zn_{0.35}Fe_{0.65})$ Fe_2O_4, integrating iron and zinc, to fortify the GelTA hydrogel matrix, thereby yielding the GelTAMNPs magnetic hydrogel. This composite was applied to the surgically exposed tumor beds following tumor excision. In contrast to previous organic polymer gels, gelatin, and TA were introduced in our experimental fabrication. A natural constituent, GelTA, was employed to craft the foundational hydrogel matrix through hydrogen bond interactions; this imparted degradable and absorbable features necessary for fillable properties during the extended treatment of the surgical wound. In contrast to the earlier studies of single iron magnetic materials, we employed an iron and zinc bimetallic-based, highly efficient magneto-thermal conversion nanoalloy $(Zn_{0.35}Fe_{0.65})$ Fe_2O_4 (MNPs), crosslinking it with the hydrogel via polyphenol-metal chelation. Consequently, the meticulously designed GelTAMNPs exhibit magneto-responsive, accessible for hypothermal therapy, and trauma-fillable capabilities. Under AMF, the magneto-converted, intensified thermal and ion bursts from GelTAMNPs could induce pyroptosis to residual tumor cells, as affirmed from in vitro to in vivo experiments. The subsequent release of cell debris and cytokines could function as a relay baton to sustain immune system activation, propelling pyroptosis-based immunotherapy. Crucially, when combined with anti-PD-1-mediated immune checkpoint blockade, this integrated therapeutic approach could enhance the efficacy of immunotherapy in addressing secondary tumors and lung metastasis post-tumor removal surgery. In essence, our endeavor introduces a sustained therapeutic platform with spatial-temporal controllability for facilitating personalized treatment plans for further remediation. This post-surgical adjuvant therapy advances precise treatment and paves the way for utilizing magnetic materials in the biomedical domain.

4. Experimental Section

Synthesis of $(Zn_{0.35}Fe_{0.65})$ Fe_2O_4 MNPs: $(Zn_{0.35}Fe_{0.65})$ Fe_2O_4 MNPs were synthesized using a previous one-pot solvothermal reduction method with slight modifications.[31] In a typical reaction, $ZnCl_2$ (2.5 mM) and $FeCl_3{\cdot}6H_2O$ (5.0 mM) were dissolved in 70 mL of ethylene glycol while being magnetically agitated (1.5 h) to form an orange homogeneous solution. Then, 0.05 mol of NH_4Ac was added to the above mixture, followed by 0.5 h of stirring to obtain a brown solution. Next, 0.03 g of chitosan was added, followed by 0.5 h of saturated stirring. Subsequently, the solution was synthesized in a Teflon-lined vessel for 24 h at 200 °C. Further, the sample was purified by centrifuging (10 137×*g*). The resulting $(Zn_{0.35}Fe_{0.65})$

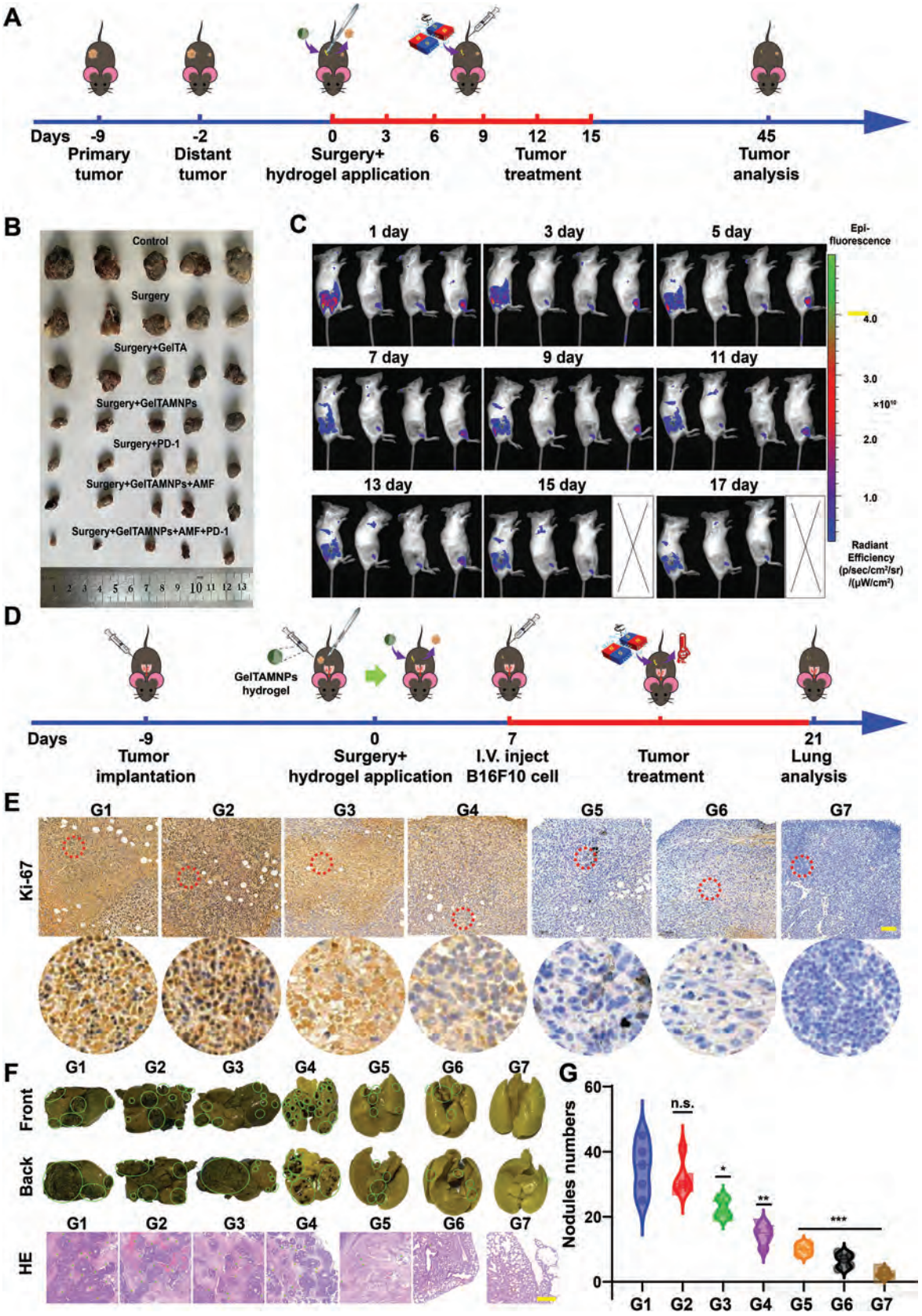

Fe_2O_4 MNPs were harvested using external magnetic force (NdFeB magnet) and dehydrated at 60 °C.

Preparation of GelTA Hydrogel: GelTA hydrogel fabrication proceeded via hydrogen bonds crosslinking. In brief, 20% *w/v* Gel was prepared at 50 °C in a water bath. Then, dropwise, a TA solution (1.5 × 10−2 g mL^{-1}) was added. After carefully removing air bubbles by ultrasonication, the GelTA precursor solution was obtained with a weight ratio of Gel: TA; 1:0.06. The obtained solution was kept at 4 °C for 4 h to induce GelTA hydrogel formation. Finally, the GelTA hydrogel was lyophilized and stored for further analysis.

Formulation of GelTAMNPs: To formulate the GelTAMNPs hydrogel, the $(Zn_{0.35}Fe_{0.65})$ Fe_2O_4 MNPs were PEGylated using SH-mPEG$_{5000}$ in a mass ratio of 1:2.25 (SH-mPEG$_{5000}$:$(Zn_{0.35}Fe_{0.65})$ Fe_2O_4 MNPs). Subsequently, the obtained PEGylated MNPs were carefully added to the GelTA precursor solution. After thorough mixing, the MNPs-doped GelTA hydrogel solution was stored in a freezer at 4 °C for 4 h to induce hydrogel formation. Finally, the Hofmeister effect was introduced to enhance the mechanical strength of hydrogel. For this purpose, the samples were soaked in ammonium sulfate (20% wt) for 12 h.

Specific Loss Power (SLP) Quantification: To evaluate the MH generated by $(Zn_{0.35}Fe_{0.65})$ Fe_2O_4 under AMF, DDCGP-06-I, an alternative magnetic field generator was employed. For this purpose, a 2 mL microtube containing 0.2 ml PBS dispersed $(Zn_{0.35}Fe_{0.65})$ Fe_2O_4 was settled in the copper coil (six-turn, Φ = 50 mm). After that, the AMF (500 kHz, 6.6 kW) was switched on, and an IR camera recorded the thermal variation. The SLP value was calculated with the following equation:

$$\mathrm{SLP} = \frac{\mathrm{CV_s}}{\mathrm{m}} \frac{\mathrm{dT}}{\mathrm{dt}} \tag{1}$$

where *C* is the volumetric heat capacity of the solvent, V_s is the sample volume, m is the mass of MNPs, and dT/dt is the initial slope of the time-dependent temperature increase curve.

Porosity Measurement: A solvent displacement method was employed to investigate the porosity of the hydrogels. In brief, the lyophilized samples were first weighed to record the initial mass. Then, absolute ethanol was added to immerse samples until total saturation. After the samples were completely immersed, the percentage of the porosity was calculated using the following equation:

$$\text{Porosity } (\%) = \frac{(W_s - W_d)}{V_s \times \rho \text{ ethanol}} \tag{2}$$

where W_s is the sample mass after immersing in ethanol, Wd is the sample mass after lyophilization, V_s is the volume of the initial sample, and ρ is the density of ethanol.

Gelation Time, Yield, and Gel Content Measurements: Gelation time reflects the time when rapid enhancement in the viscosity of the hydrogel is observed. As for the GelTA hydrogel, the gelation time was analyzed as a function of TA concentration via the tube inversion method. After adding the TA to the gelatin solution, the gelation time was determined by recording when the contents stopped flowing. For yield determination, the GelTA hydrogels were first prepared using four different concentrations of Gel (w/v) solution, and then the hydrogels were dried in the oven at 60 °C. After drying, the weight of hydrogels was determined to calculate the yield following this equation:

$$\text{Yield } (\%) = \frac{W_{dh}}{W_{ig} + W_{iT} + W_{iM}} \times 100\% \tag{3}$$

where W_{dh} is the weight of the dried hydrogel, W_{ig} is the initial weight of Gel, W_{iT} is the initial weight of TA, and W_{iM} is the initial weight of the MNPs.

The Gel content was calculated to determine the optimal ratio of Gel to TA based on the maximum interaction between these two compounds and hydrogel formation. For this purpose, dried hydrogels, prepared using four different concentrations of TA, were first weighed and then immersed in the PBS (pH 7.4) for 4 h at 40 °C. After removing the buffer, the sample was dehydrated in the oven at 60 °C and weighed. The percentage of Gel content was calculated via the equation:

$$\text{Gel content } (\%) = \frac{W_{dh}}{W_{ih}} \times 100\% \tag{4}$$

where W_{dh} is the weight of the dried hydrogel, and W_{ih} is the initial weight of the hydrogel.

The initial wet weights of freshly prepared samples were recorded for the IWC analyses. Then, the samples were fully dehydrated, and their weights were remeasured to calculate the IWC using the equation:

$$\text{IWC } (\%) = \frac{W_{wh} - W_{ds}}{W_{wh}} \times 100\% \tag{5}$$

where W_{wh} is the weight of freshly prepared hydrogel samples and W_{ds} is the weight of fully dehydrated samples.

To study the hydrogel's swelling behavior, 50 mg of dehydrated hydrogel was incubated in PBS (pH 7.4) at 37 °C. At pre-determined time points, the weight of the swelled hydrogel was measured after removing excess water from the surface of the hydrogel by blotting it very gently on filter paper. The percentage of swelling was calculated using the equation:

$$\text{Swelling } (\%) = \frac{W_s - W_d}{W_d} \times 100\% \tag{6}$$

where W_s is the weight of the swelled hydrogel, and W_d is the weight of the dry hydrogel.

Dehydrated hydrogels (50 mg) were first incubated in PBS (pH 7.4) at 37 °C for 48 h to measure water retention. The samples were transferred to clean dishes after the buffer was absorbed. The surface of the hydrogels was gently dried using filter paper; the soaked filter paper weight was measured at pre-determined time points. Finally, the hydrogels were dried in the oven at 60 °C until a constant weight was obtained. Finally, water retention was calculated according to the equation:

$$\text{Water retention } (\%) = \frac{M_W - M_C}{M_C} \times 100\% \tag{7}$$

where M_w is the weight of the filter paper containing the surface water of the gel, and M_c is the constant weight after dehydrating at 60 °C.

Figure 8. Therapy of post-surgery distant tumor and tumor metastasis inhibition. A) Schematic depiction of the tumor induction process followed by surgery and GelTAMNPs application to the wound. B) Fluorescence in vivo imaging of RhB-labeled GelTAMNPs. The experiments were carried out with four mice per group; however, one mouse had to be sacrificed due to the low activity of GelTAMNPs without AMF. Hence, its images are missing on the 15th and 17th day. C) Digital photodocumentation of tumors excised from mice at the experimental endpoint. D) Schematic depiction of the tumor induction process followed by surgery and GelTAMNPs application to the wound and subsequent analysis of lung tissues. E) Immunohistochemistry showing expression of Ki-67 in the tumor tissues; Scale bars, 100 µm. F) Digital photo and documentation of B16F10 cells metastasis into lungs stained with Bouin's reagent and H&E images of different groups; Scale bars, 500 µm. Images are representative photographs from five biologically independent replicates. G) Pulmonary metastatic nodules determined in individual groups: G1: control, G2: surgery, G3: surgery + GelTA, G4: surgery + GelTAMNPs, G5: surgery + PD-1, G6: surgery + GelTAMNPs + AMF, and G7: surgery + GelTAMNPs + AMF + PD-1. Statistical significances were calculated via the Student's *t*-test. $^{*}p < 0.05$, $^{**}p < 0.01$, and $^{***}p < 0.001$.

For the degradation study, mass loss was calculated by comparing the initial dried mass and the mass of dehydrated gels after immersing them in PBS (pH 7.4). Hydrogels were taken out for weighing at each point after baking them in the oven. The percentage of the degradation was calculated using the equation:

$$\text{Degradation } (\%) = \frac{W_1 - W_2}{W_1} \times 100\% \quad (8)$$

where W_1 is the weight of the initial dried mass, and W_2 is the weight of the re-dried hydrogel mass.

DMA Measurement: DMA 242 C/1/G (Netzsch, Selb, Germany) was utilized to assess the elastic and loss moduli of the hydrogels. The measurements were performed in compression mode at a frequency of 10 Hz at temperatures spanning from 20 to 120 °C with a cooling rate of 3 °C min^{-1}. A constant load of 2 N and an amplitude of 20 m were applied. The measurements were conducted at a strain (γ) of 1% and a frequency (ω) of 6.28 rad s^{-1}. Both heating and cooling processes had rates of ±0.5 °C min^{-1}.

Evaluation of Ion Release from GelTAMNPs: For evaluating ion release from hydrogel, TME simulation buffers with different pH values (4.2, 5.5, and 7.2) were prepared. These buffers were placed in a constant temperature water bath set to 37 °C and then used to mimic in vivo conditions for determining ion release and degradation of hydrogels. The hydrogel blocks were prepared and placed into buffers with differing pH. The buffers were sampled at different time points (3 h, 6 h, 12 h, 1 d, 2 d, 4 d, 8 d, and16 d), and the released ions were quantified using ICP-MS (7700x, Agilent, Santa Clara, CA, USA).

Cell Culture: An RPMI-1640 cell culture medium supplemented with penicillin/streptomycin (100 units/mL) and 10% fetal bovine serum (FBS) was used for B16F10 murine melanoma cell culturing. A 0.25% trypsin–EDTA solution was used to harvest cells for subsequent analyses.

Evaluation of Cellular Uptake of GelTA-($Zn_{0.35}Fe_{0.65}$) Fe_2O_4: To examine cellular uptake, a fluorescein isothiocyanate (FITC)-labeled GelTAMNPs was prepared by adding free FITC into the GelTAMNPs aqueous dispersion. The labeled GelTAMNPs were collected by centrifugation and purified by washinfg with PBS. GelTAMNPs samples were prepared as lyophilized powder for all cell experiments and diluted before administration. For confocal laser scanning microscopy (CLSM) experiments, dishes were seeded with B16F10 cells (10^5 cells/well); the cells were incubated overnight. A fresh culture medium containing FITC-labeled GelTAMNPs (9 μg mL^{-1}) was added to the dishes, followed by a 6 h incubation. Then, the cells were rinsed with PBS to remove any non-internalized material. Further, LysoTracker Red and 4′,6-diamidino-2-phenylindole (DAPI) were used to stain the endolysosomal compartments and nuclei. Finally, the micrographs were captured with a Leica SP 8 CLSM (Leica, Wetzlar, Germany) using the excitation wavelengths of 358 nm (DAPI) and 490 nm (FITC).

In Vitro Cytotoxicity Testing: A CCK-8 assay was utilized to examine the in vitro cytotoxicity of GelTAMNPs and the GelTAMNPs exposed to AMF for 10 min. For this, a 96-well plate was seeded with B16F10 cells at a density of 5×10^4 cells/ well. After that, cells were administered with various concentrations of GelTAMNPs (0, 0.2, 0.4, 0.6, and 0.8 mg mL^{-1}). After 24 h incubation, CCK-8 was added to the wells according to the manufacturer's instructions, and cell viability was determined at 450 nm.

In Vitro Analysis of Cellular Response to GelTAMNPs: B16F10 cells were cultured in 6-well plates of 2 × 105/well density. The cells were observed under a bright field and photographed after different treatments. Besides, the cells were stained with an Annexin V-FITC apoptosis detection kit and analyzed using flow cytometry.

Total proteins were extracted from treated cells using a cold RIPA lysis buffer to investigate the expression of proteins involved in pyroptosis (GSDME, GSDMD, and NLRP3). After separating the proteins on electrophoresis and transferring them onto the polyvinylidene fluoride membrane, immunoblotting was performed using rabbit polyclonal anti-GSDMD (cat. no. #93709, Cell Signaling Technology, Danvers, MA, USA), anti-GSDME (cat. no. 67731-1-1G, Proteintech, Rosemont, IL, USA) and rabbit polyclonal anti-NLRP3 (cat. no. 19771-1-AP, Proteintech, Rosemont, IL, USA) antibodies (both diluted to 1:1000). After incubation at 4 °C, membranes were washed and incubated with horseradish peroxidase (HRP)-conjugated goat anti-rabbit secondary antibody (dilution 1:3000, Abcam, Cambridge, UK, cat. no. ab97051). The membranes were visualized using ChampChemi 610 plus (Beijing Sage Creation, Science, Beijing, China). Densitometric analysis of western blots was performed using ImageJ (NIH, Bethesda, MA, USA).

Further, wound-healing and transwell assays were performed to evaluate tumor cell invasion. For this purpose, B16F10 cells were seeded in a six-well plate (2×10^5 of cells/ well). Then, the cells were incubated with PBS, GelTA, MNPs, and GelTAMNPs, respectively, and further divided into two groups; these groups were either i) exposed or ii) not exposed to AMF. For the wound-healing assay, cells were cultured in an FBS-free medium; a monolayer was formed, and a wound was created by scratching it with a sterile pipette tip. Wound closing was evaluated at 12 and 24 h time points. In the transwell assay, the treated cells seeded in the upper chambers were cultured with an FBS-free medium. In contrast, the lower chambers contained FBS to induce cell invasion. After 24 h, the cells that migrated to the lower chamber were fixed and stained using 0.1% crystal violet and observed under a microscope. HMGB1, LDH, and ATP expressions were detected as biomarkers to evaluate the ICD action following pyroptosis. The B16F10 cells were seeded until 80% confluence was inoculated with different treatments, including PBS, GelTAMNPs (0.5 mg mL^{-1}), and GelTAMNPs (0.5 mg mL^{-1}) + AMF. After 24 h, cells were conducted to determine the release of HMGB1, LDH, and ATP following the kits procedure.

Animals and Melanoma Model: Female C57 mice were purchased from Huafukang Biological Technology (Beijing, China). All procedures related to the animal model used in this study were per the standard protocol approved by Tianjin University. All the animals received humane care in compliance with the institution's guidelines for maintaining and using laboratory animals in research. Tumors were induced by subcutaneous injection of B16F10 cells (5×10^6) into the flank regions. Tumor sizes were measured periodically using a slide caliper. After 10 days of tumor induction, surgical interventions (partial removal of tumor tissues leaving ≈5% of residual tumor mass) were performed.

In Vivo Multimodal Imaging: For in vivo CT imaging, 200 μL homogenized GelTAMNPs (25 mg k^{-1}g) were injected intratumorally. Subsequently, an X-ray Micro CT scanner (Quantum FX, PerkinElmer, Hopkinton, MA, USA) was used for imaging (before and after injection) after anesthetizing.

For in vivo IR thermal imaging, the tumor-bearing mice were administered with saline or 30 mg k^{-1}g of GelTAMNPs by direct intratumoral injections. After exposing the mice to AMF, hyperthermia images were acquired using an IR thermal imaging system (Fluke TiR). The mice were fixed in the copper coil, and the thermal videos were recorded for further analysis at the following time points: 20, 40, 60, 80, 100, 120, 140, and 160 s.

In Vivo Antitumor Efficacy of GelTAMNPs: To evaluate the antitumor activity of GelTAMNPs, the mice were segregated into seven distinct groups (five mice per group). The groups were: G1, control; G2, surgery; G3, surgery + GelTA; G4 surgery + GelTAMNPs; G5, surgery + PD-1; G6, surgery + GelTAMNPs + AMF; and G7, surgery + GelTAMNPs + AMF + PD-1. After surgical resection, wounds were filled with individual hydrogel-based formulations. During this process, samples had to be thoroughly monitored to ensure the open wounds were filled with the hydrogel formulations without developing air bubbles. The wounds were stitched after hydrogel application. For AMF exposure, the AMF frequency (f) of 309 kHz and the magnetic field intensity (H) of 40 KA m^{-1} ($f \times H < 10^9$) were applied for 10 min.

The double-tumor-bearing model was established to evaluate the possible abscopal antitumor efficiency of GelTAMNPs. For this purpose, the distant tumor was induced in the flank one week after the induction and growth of the primary tumor in the second flank. After this period, primary tumors were surgically removed, and the resection cavities were filled with hydrogels, as described above. The distant secondary tumors and lung metastases were examined after that. For the lung metastasis analysis, the lung tissues were excised, and the pulmonary metastatic nodules were stained with Bouin's solution. The tumor sizes and body weight variations

were recorded in all the experiments every other day. The volume of the tumor was assessed as (width^2×length)/2.

Analysis of T Cells in B16F10 Tumors by Flow Cytometry: To analyze the immune cells in tumors, tissues were collected and dissociated. After dissociation, the cells were washed with PBS and stained with the following fluorescently labeled antibodies: anti-CD3 PE (1:1000, Abcam, cat. no. ab22268), anti-CD4 FITC (1:250, Abcam, cat. no. ab59474), anti-CD8 APC (1:2500, Abcam, cat. no. ab256309), anti-CD11c PerCP/Cy5.5 (1:200, Abcam, cat. no. ab111469), anti-CD80 PE/Cy5 (1:1000, Abcam, cat. no. ab95548), or anti-CD86 APC (1:1000, Abcam, cat. no. ab218757). Following immunolabeling, cell surface markers were analyzed through flow cytometry using the LSRFortessa by BD Biosciences. Subsequently, the data obtained was analyzed using the FlowJo software.

In Vivo Imaging of the Fluorescently Labeled GelTAMNPs: To study the retention of GelTAMNPs, the RhB-labeled GelTAMNPs were first synthesized. The GelTAMNPs were conjugated to the amine group with the carboxyl group of the RhB, resulting in an ester derivative, which is stable under physiological pH conditions. Typically, 0.4 g GelTAMNPs were dissolved in 10 mL PBS. Then, 4 mg of RhB dissolved in 0.4 mL dimethyl sulfoxide was added into the GelTAMNPs solution and mixed thoroughly. The reaction was kept at room temperature in the dark overnight. Excess RhB was removed by dialysis at room temperature for 48 h. The labeled GelTAMNPs were then freeze-dried. Finally, the mice were administered with RhB-labeled GelTAMNPs after surgery and subjected to fluorescence imaging at different time points (1, 3, 5, 7, 9, 11, 13, 15, 17 d) using a small animal in vivo imaging system (Perkin Elmer, Waltham, MA, USA).

Tissue Immunolabeling and Staining: After excision, the tumor samples were fixed in 4% paraformaldehyde and embedded into paraffin blocks. After tissue sectioning, the slides were immunolabeled using primary antibodies against: IL-18 (1:2000, Abcam, cat. no. ab223293), IL-1β (1:500, Abcam, cat. no. ab283818), CRT (1:500, Abcam, cat. no: ab92516), HMGB-1 (1:400, Abcam, cat. no. ab79823), and anti-Ki-67 (1:1000, Abcam, cat. no. ab15580). After incubation and washing, the tissues were labeled with either HRP-conjugated secondary antibodies (1:1000, Abcam, cat. no. ab7090, for IL-18, IL-1β, and Ki-67) or Cy5.5-labeled secondary antibodies (1:1000, Abcam, cat. no. ab6947, for CRT and HMGB-1). In addition, slides were also stained using H&E and TUNEL assays. Finally, all the tissues were observed under a Panoramic 250 Flash III microscope (3DHISTECH, Budapest, Hungary).

Acute Toxicity Test of GelTAMNPs: To examine the hematological and blood biochemical parameters, an automatic hematological analyzer (Mindray BC6800, Mindray, Shenzhen, China) was employed. The serum biochemical parameters analyzed in this study were: alanine transaminase (ALT); aspartate transaminase (AST); total protein (TP); albumin (ALB); creatinine (CREA); alkaline phosphatase (ALP); uric acid (UA), and urea.

Hemolysis Test of GelTAMNPs: After diluting the blood samples with PBS, RBCs were isolated by centrifugation. Then, 200 µL of the diluted RBCs were mixed with 1 mL of deionized water (positive control), PBS (negative control), or different concentrations (20–200 mg mL^{-1}) of GelTAMNPs. After incubation at 37 °C for 2 h, the samples were centrifuged and collected. The supernatants were transferred into a 96-well plate to measure the absorbance of the released hemoglobin at 570 nm. The percent hemolysis of the RBCs was calculated according to the following equation:

$$\text{Hemolysis ratio } (\%) = \frac{A_{(Sample,\ 570\ nm)} - A_{(negative,570\ nm)}}{mean\ value\ of\ \left[A_{(Sample,\ 570\ nm)} - A_{(negative,570\ nm)}\right]} \times 100\% \quad (9)$$

Statistical Analysis: Data are shown as mean ± SD. One-way analysis of variance (ANOVA) was used to determine the significance of differences among groups. The Student's *t*-test was applied to compare the results of the two groups. *Denotes statistical significance at $p < 0.05$, ** denotes $p < 0.01$, and *** denotes $p < 0.001$. GraphPad Prism 9.3.0 for Windows (GraphPad Software, San Diego, USA) was used for statistical analyses.

Supporting Information

Supporting Information is available from the Wiley Online Library or from the author.

Acknowledgements

This work was supported by the Young Elite Scientists Sponsorship Program by Tianjin University (grant number 0701320001); the Major Special Projects (grant number 0402080005); the National Key R&D Program of China (grant number 2019YFA0905104); and the Natural Science Foundation of Guangdong Province (grant number 2019A1515011498). ZH would like to express his gratitude to the Czech Science Foundation (project no. 23-04740M).

Open access publishing facilitated by Mendelova univerzita v Brne, as part of the Wiley - CzechELib agreement.

Conflict of Interest

The authors declare no conflict of interest.

Author Contributions

S.W. and H.J. contributed equally to this work. N.L. conceptualized the idea for the study; designed methodology; and acquired resources. V.A. performed validation and wrote, reviewed, and edited the final manuscript. S.W. and H.J. performed investigation and supervision and wrote the original draft. Y.Z. and R.Y. performed investigation and project administration. Z.H. and S.K. wrote the original draft and contributed to the study design. L.V. and X.L. performed investigation. All authors have given their approval to the final version of the manuscript.

Data Availability Statement

The data that support the findings of this study are available from the corresponding author upon reasonable request.

Keywords

magnetic nanoparticles, magnetocaloric-responsive hydrogel, post-operation tumor recurrence and metastasis, pyroptosis-relay-immunotherapy

Received: November 11, 2023
Revised: January 2, 2024
Published online: February 5, 2024

[1] J. Donington, L. Schumacher, J. Yanagawa, *J. Clin. Oncol.* **2022**, *40*, 530.
[2] C. Peitzsch, A. Tyutyunnykova, K. Pantel, A. Dubrovska, *Semin. Cancer Biol.* **2017**, *44*, 10.
[3] L. Borriello, A. Coste, B. Traub, V. P. Sharma, G. S. Karagiannis, Y. Lin, Y. Wang, X. Ye, C. L. Duran, X. Chen, M. Friedman, M. S. Sosa, D. Sun, E. Dalla, D. K. Singh, M. H. Oktay, J. A. Aguirre-Ghiso, J. S. Condeelis, D. Entenberg, *Nat. Commun.* **2022**, *13*, 626.
[4] D. Lin, L. Shen, M. Luo, K. Zhang, J. Li, Q. Yang, F. Zhu, D. Zhou, S. Zheng, Y. Chen, J. Zhou, *Signal Transduct. Target Ther.* **2021**, *6*, 404.
[5] H. Wu, C. Huang, L. Wang, Q. Li, Y. Li, L. Zhang, D. Zhu, *Chin. Chem. Lett.* **2022**, *33*, 5035.

[6] B. You, T. Xia, M. Gu, Z. Zhang, Q. Zhang, J. Shen, Y. Fan, H. Yao, S. Pan, Y. Lu, T. Cheng, Z. Yang, X. He, H. Zhang, M. Shi, D. Liu, Y. You, *Cancer Res.* **2022**, *82*, 846.
[7] T. G. Phan, P. I. Croucher, *Nat. Rev. Cancer* **2020**, *20*, 398.
[8] L. de la Cruz-Merino, A. Illescas-Vacas, A. Grueso-López, A. Barco-Sánchez, C. Míguez-Sánchez, *Front Immunol.* **2014**, *5*, 102.
[9] S. R. Yu, J. Wei, X. P. Qian, B. R. Liu, *Ai zheng = Aizheng = Chin. J. Cancer* **2009**, *28*, 1225.
[10] M. A. Marsili, M. K. Robinson, G. A. Truitt, E. F. Wheelock, *Cancer Res.* **1983**, *43*, 15.
[11] G. Kroemer, L. Galluzzi, O. Kepp, L. Zitvogel, *Annu. Rev. Immunol.* **2013**, *31*, 51.
[12] X. Si, G. Ji, S. Ma, H. Chen, Z. Shi, Y. Zhang, Z. Tang, W. Song, X. Chen, *J. Control Release* **2023**, *353*, 289.
[13] M. Moshirfar, D. A. Fuhriman, A. Ali, V. Odayar, Y. C. Ronquillo, P. C. Hoopes, *J. Clin. Med.* **2022**, *11*, 4861.
[14] D. C. Hinshaw, L. A. Shevde, *Cancer Res.* **2019**, *79*, 4557.
[15] H. E. Barker, J. T. Paget, A. A. Khan, K. J. Harrington, *Nat. Rev. Cancer* **2015**, *15*, 409.
[16] T. Du, J. Gao, P. Li, Y. Wang, Q. Qi, X. Liu, J. Li, C. Wang, L. Du, *Clin. Transl. Med.* **2021**, *11*, e492.
[17] Y. Fang, S. Tian, Y. Pan, W. Li, Q. Wang, Y. Tang, T. Yu, X. Wu, Y. Shi, P. Ma, Y. Shu, *Biomed. Pharmacother.* **2020**, *121*, 109595.
[18] J. Shi, Y. Zhao, K. Wang, X. Shi, Y. Wang, H. Huang, Y. Zhuang, T. Cai, F. Wang, F. Shao, *Nature* **2015**, *526*, 660.
[19] J. Shi, W. Gao, F. Shao, *Trends Biochem. Sci.* **2017**, *42*, 245.
[20] Y. Tan, Q. Chen, X. Li, Z. Zeng, W. Xiong, G. Li, X. Li, J. Yang, B. Xiang, M. Yi, *J. Exp. Clin. Cancer Res.* **2021**, *40*, 153.
[21] A. Gardner, B. Ruffell, *Trends Immunol.* **2016**, *37*, 855.
[22] T. Wang, D. Wang, H. Yu, B. Feng, F. Zhou, H. Zhang, L. Zhou, S. Jiao, Y. Li, *Nat. Commun.* **2018**, *9*, 1532.
[23] J. Zhang, C. Chen, A. Li, W. Jing, P. Sun, X. Huang, Y. Liu, S. Zhang, W. Du, R. Zhang, Y. Liu, A. Gong, J. Wu, X. Jiang, *Nat. Nanotechnol.* **2021**, *16*, 538.
[24] O. Hasturk, K. E. Jordan, J. Choi, D. L. Kaplan, *Biomaterials* **2020**, *232*, 119720.
[25] X. Lin, X. Xing, S. Li, X. Wu, Q. Jia, H. Tu, H. Bian, A. Lu, L. Zhang, H. Yang, B. Duan, *Adv. Funct. Mater.* **2022**, *32*, 2112685.
[26] Z. Ahmadian, A. Correia, M. Hasany, P. Figueiredo, F. Dobakhti, M. R. Eskandari, S. H. Hosseini, R. Abiri, S. Khorshid, J. Hirvonen, H. A. Santos, M. A. Shahbazi, *Adv. Healthcare Mater.* **2021**, *10*, e2001122.
[27] Z. Zhou, J. Xiao, S. Guan, Z. Geng, R. Zhao, B. Gao, *Carbohydr. Polym.* **2022**, *285*, 119235.
[28] B. Ding, P. Zheng, P. Ma, J. Lin, *Adv. Mater.* **2020**, *32*, 1905823.
[29] Z. Li, Y. Li, C. Chen, Y. Cheng, *J. Control Release* **2021**, *335*, 541.
[30] J. T. Jang, H. Nah, J. H. Lee, S. H. Moon, M. G. Kim, J. Cheon, *Angew. Chem., Int. Ed. Engl.* **2009**, *48*, 1234.
[31] X. Liu, Y. Q. Huo, L. K. Yan, N. Fan, K. Z. Cai, Z. M. Su, *Chemistry* **2020**, *26*, 14397.